JOURNAL OF APPLIED PHYSICS VOLUME 42, NUMBER 2 FEBRUARY 1971

Metal-Oxide-Metal (M-O-M) Detector*

S. P. KWOK, G. I. HADDAD, AND G. LOBOV†

Electron Physics Laboratory, Department of Electrical Engineering, The University of Michigan, Ann Arbor, Michigan 48104

(Received 15 July 1970)

The properties of a metal-oxide-metal (M-O-M) tunneling detector are presented and the parameters influencing its operation are discussed. The theory of operation and experimental results for small as well as large signals are presented. The polarity reversal at large-signal levels is predicted theoretically and observed experimentally.

I. INTRODUCTION

The voltage-current characteristic of a metal-oxide-metal or metal-insulator-metal structure with nonsuperconducting metals has been widely studied using a phenomenological potential barrier and an independent electron model.[1-5] This method has been commonly used to analyze the experimental results where some parameters are empirically determined. A phenomenological model is also employed in the work presented here.

By virtue of the fast tunneling time of electrons through a thin barrier, the M-O-M structure can be used as a millimeter, submillimeter, and shorter wavelength room-temperature detector.

Hartman[6] calculated the transmission time of a free electron wave packet tunneling through a potential barrier of a thin film sandwiched between two similar metal electrodes. He showed that for a film thickness greater than several interatomic distances (3-5 Å) the transmission time is approximately given by

$$t=h/2\pi(\eta\phi)^{1/2}, \tag{1}$$

where h is Planck's constant, η is the Fermi energy of the metal, and ϕ is the work function of the metal. This transmission time is on the order of 10^{-16} sec and is independent of the insulating film thickness for a wide variety of metals. This transmission time is different from the RC time constant of the structure and has been sometimes mistaken to be the tunneling time of electrons through the potential barrier. The main difficulty in assuming this transmission time to be the tunneling time of electrons through a potential barrier is the inadequacy of the implicit free electron assumption. Fredkin and Wannier[7] analyzed the motion of an electron wave packet in a semiconductor and found the tunneling time to be explicitly dependent on the junction potential width.

The RC time constant arising from tunneling will be taken as the transit time of the tunneling process as did Thornber *et al.*[8] Lewicki and Mead[9] measured and extrapolated the RC constant of an Al-AlN-Mg structure for a 10-Å film to be about 10^{-12} sec. Experimentally, Hocker *et al.*[10] and Green[11] observed frequency mixing of the HCN, 337-μm laser line with the thirteenth harmonic of a V-band klystron using a point-contact metal-oxide-metal structure. This shows the RC time constant to be on the order of 10^{-12} sec or smaller.

Coleman and Green[11,12] pointed out the small-signal detection capability of an M-O-M structure with dissimilar metal electrodes without a dc bias. They also calculated the small-signal detection properties using the generalized I-V relation due to Simmons[2,3] and pointed out the possibility of a large-signal polarity reversal. They also measured this polarity reversal.

In this report a different approach for calculating the small-signal detection properties using the idealized trapezoidal potential barrier was employed. The results are in agreement with those obtained by Green.[11] Furthermore, calculations which include a parabolic image potential as a small perturbation on the trapezoidal barrier have been performed. These give rise to an additional term in the detected signal which predicts polarity reversal at a large-signal level, though at such signal levels the small-signal analysis becomes inadequate. More exact calculations of the detected current with the image potential included in the potential barrier were carried out on a computer. Both the small-signal and the large-signal detection properties were calculated. These are supported by experimental results.

II. SMALL-SIGNAL THEORY

A. I-V Characteristic

The transmission coefficient of electrons having energy E to tunnel through a potential barrier $U(x)$ may be expressed through the well-known WKB approximation[13] as

$$D(E)=\exp\left(-2\int_a^b k dx\right), \tag{2}$$

where a, b are the classical turning points, $k=\{2m/\hbar^2[U(x)-E]\}^{1/2}$, and m is the electronic mass, provided that $|k'(x)|\ll|k(x)|^2$, i.e., $U(x)$ is a slowly varying function of x, for x well within the region $a<x<b$. This is illustrated in Fig. 1. For a one-dimensional problem Eq. (2) becomes

$$D(E_x)=\exp\left(-\frac{4\pi}{h}\int_{s_1}^{s_2}\{2m[U(x)-E_x]\}^{1/2}dx\right), \tag{3}$$

where $E_x=(1/2)mv_x^2$, v_x is the velocity component in the x direction, and s_1, s_2 are the classical turning points. The rate of electrons tunneling from side 1 to side 2 is given by

$$N_1=\int_0^{v_m} v_x n(v_x)D(E_x)dv_x=m^{-1}\int_0^{E_m} n(v_x)D(E_x)dE_x, \quad (4)$$

where $E_m=(1/2)mv_m^2$, v_m is the maximum x component of velocity of electrons,

$$n(v_x)=\frac{2m^3}{h^3}\int_{-\infty}^{\infty}\int_{-\infty}^{\infty} f(E)dv_y dv_z, \quad (5)$$

$f(E)$ is the Fermi–Dirac distribution function, and v_y, v_z are the y- and z-velocity components of electrons.

Hence

$$N_1=\frac{4\pi m}{h^3}\int_0^{E_m} D(E_x)dE_x\int_{E_x}^{\infty} f(E)dE.$$

Similarly, the rate of electrons tunneling from side 2 to side 1 is

$$N_2=\frac{4\pi m}{h^3}\int_0^{E_m} D(E_x)dE_x\int_{E_x}^{\infty} f(E+eV)dE,$$

where V is the applied bias voltage. The net rate of electron flow from side 1 to side 2 is then

$$N=N_1-N_2=\frac{4\pi m}{h^3}\int_0^{E_m} D(E_x)dE_x \times\int_{E_x}^{\infty}[f(E)-f(E+eV)]dE. \quad (6)$$

The tunneling-current density is given by

$$I=I_0\int_0^{E_m}\exp\left(-\frac{4\pi}{h}\int_{s1}^{s2}[U(x)-E_x]^{1/2}dx\right)\xi dE_x, \quad (7)$$

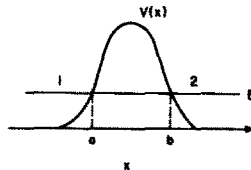

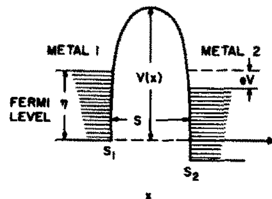

FIG. 1. Metal–oxide–metal structure.

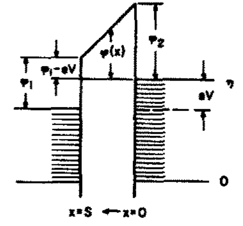

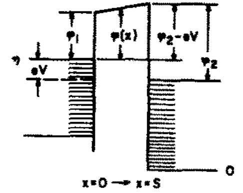

FIG. 2. Trapezoidal barrier model of the M–O–M structure.

where

$$\xi=\int_{E_x}^{\infty}[f(E)-f(E+eV)]dE = eV-kT\ln\left(\frac{1+\exp(E-\eta+eV/kT)}{1+\exp(E-\eta/kT)}\right)$$

and

$$I_0=4\pi me/h^3.$$

The integral in Eq. (7) cannot be evaluated in closed form. However, for the case of $T=0°\mathrm{K}$, ξ simplifies to

$$\xi=eV, \quad \text{for } E_x<\eta-eV$$
$$\xi=\eta-E_x, \quad \text{for } \eta-eV<E_x<\eta$$
$$\xi=0, \quad \text{for } E_x>\eta. \quad (8)$$

Then Eq. (7) becomes

$$I=I_0\left(\int_0^{\eta-eV} eVD(E_x)dE_x+\int_{\eta-eV}^{\eta}(\eta-E_x)D(E_x)dE_x\right). \quad (9)$$

For small signals, eV, Eqs. (3) and (9) may be approximated by a Taylor expansion as

$$D(E_x)=A_0+A_1(eV)+A_2(eV)^2 \quad (10)$$

and

$$I=I_0[a_1(eV)+a_2(eV)^2+a_3(eV)^3]. \quad (11)$$

It is not necessary to include a third-power term in Eq. (10) since it appears multiplied by eV in Eq. (9). Upon substitution of Eq. (10), Eq. (9) becomes

$$I=I_0\left(\int_0^{\eta-eV} eV[A_0+A_1(eV)+A_2(eV)^2]dE_x +\int_{\eta-eV}^{\eta}(\eta-E_x)[A_0+A_1(eV)+A_2(eV)^2]dE_x\right). \quad (12)$$

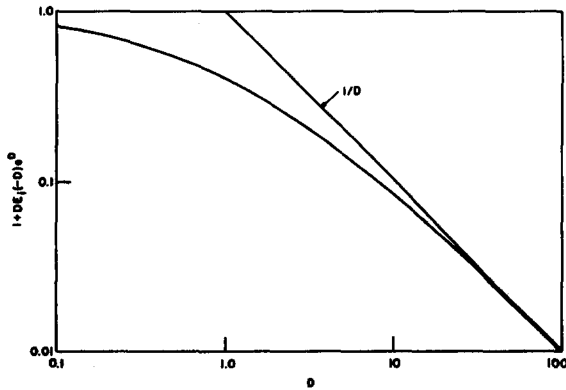

FIG. 3. The function $1+DE_i(-D)e^D$ vs D.

Comparing the coefficients with those of Eq. (11)[14] the following is obtained

$$a_1=\int_0^{\eta} A_0 dE_x, \tag{13}$$

$$a_2=\int_0^{\eta} A_1 dE_x-\tfrac{1}{2}A_0(\eta) \tag{14}$$

and

$$a_3=\int_0^{\eta} A_2 dE_x-\tfrac{1}{2}A_1(\eta)+\tfrac{1}{6}A_0'(\eta). \tag{15}$$

The potential barrier of a thin film between two dissimilar metal electrodes without an image potential is given by a trapezoidal barrier as shown in Fig. 2.

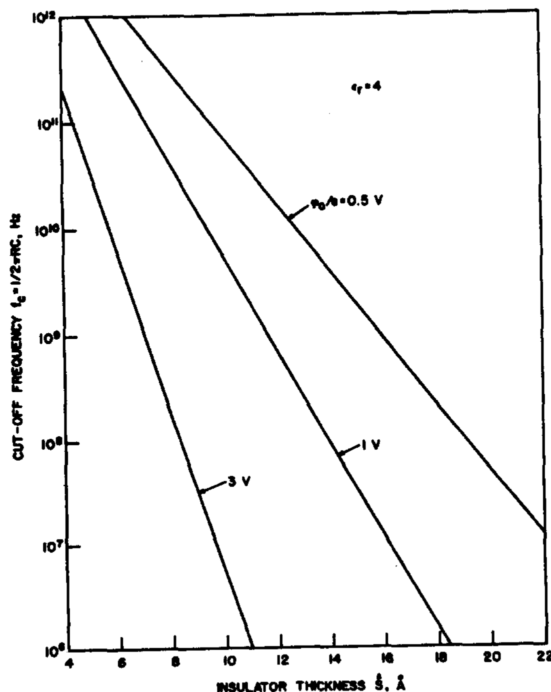

FIG. 4. Cutoff frequency vs insulator thickness.

A forward bias is defined to be a positive bias applied to the metal of a lower work function and vice versa. The potential barrier is

$$U(x)=\phi(x)+\eta. \tag{16}$$

Referring to Figs. 2 the following is written:

$$\phi_F=\phi_0+(\Delta\phi/2)-(\Delta\phi+eV)(x/s) \tag{17}$$

for forward bias and

$$\phi_R=\phi_0+(-\Delta\phi/2)-[(-\Delta\phi)+eV](x/s) \tag{18}$$

for reverse bias, where

$$\phi_0=(\phi_1+\phi_2)/2,$$

$$\Delta\phi=\phi_2-\phi_1, \qquad \phi_2>\phi_1,$$

and ϕ_i is the work function of the ith metal.

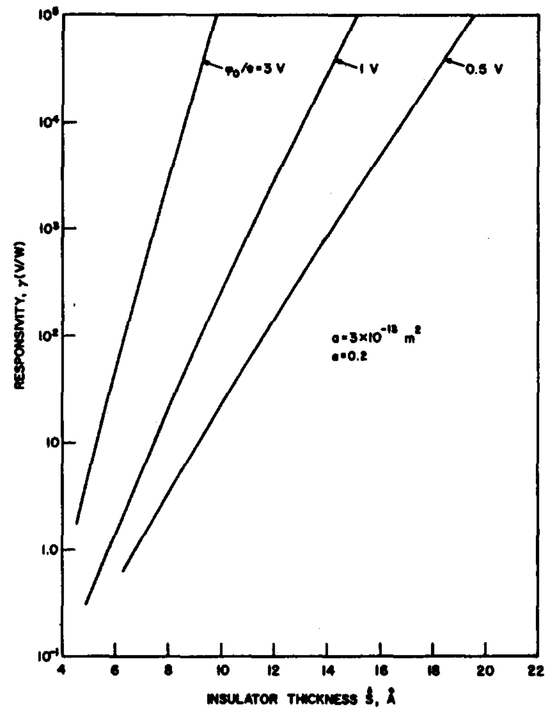

FIG. 5. Responsivity vs insulator thickness.

It is noted that $\phi_R(x)$ can be obtained from $\phi_F(x)$ by changing the sign of $\Delta\phi$, provided the reference of x is simultaneously changed as shown in Fig. 2. Substituting Eqs. (16) and (17) into Eq. (3), for forward bias, gives

$$D(E_x)=e^{\theta}$$

$$=\exp\left[-\frac{4\pi(2m)^{1/2}}{h}s\int_0^1\left(\eta-E_x+\phi_0+\tfrac{1}{2}(\Delta\phi)-(\Delta\phi+eV)\frac{x}{s}\right)^{1/2}d\left(\frac{x}{s}\right)\right]. \tag{19}$$

Letting $B=[4\pi(2m)^{1/2}/h]s$ and $L=\eta-E_x+\phi_0$ and assuming $L\gg(\Delta\phi/2)-(\Delta\phi+eV)(x/s)$, the exponent is written approximately as

$$\rho=-BL^{1/2}\int_0^1\left[1+\frac{(\Delta\phi/2)-(\Delta\phi+eV)(x/s)}{2L}-\frac{[(\Delta\phi/2)-(\Delta\phi+eV)(x/s)]^2}{8L^2}\right]d\left(\frac{x}{s}\right)+\int_0^1\left[\frac{[(\Delta\phi/2)-(\Delta\phi+eV)(x/s)]^3}{16L^3}\right]d\left(\frac{x}{s}\right). \quad (20)$$

If only terms which are proportional to eV, $\Delta\phi$, $\Delta\phi eV$, $(eV)^2$, and $\Delta\phi(eV)^2$ are kept, the exponent becomes

$$\rho=-BL^{1/2}+\frac{B(eV)}{4L^{1/2}}+\frac{\Delta\phi B(eV)}{48L^{3/2}}+\frac{B(eV)^2}{24L^{3/2}}+\frac{\Delta\phi B(eV)^2}{64L^{5/2}}. \quad (21)$$

Hence,

$$D(E_x)=\exp(-BL^{1/2})\times\left(1+\frac{B(eV)}{4L^{1/2}}+\frac{\Delta\phi B(eV)}{48L^{3/2}}+\frac{B(eV)^2}{24L^{3/2}}+\frac{\Delta\phi B(eV)^2}{64L^{5/2}}+\frac{B^2(eV)^2}{32L}+\frac{B^2\Delta\phi(eV)^2}{192L^2}\right), \quad (22)$$

where $BeV/4L^{1/2}\ll1$ has been assumed for the expansion. Rearranging terms in Eq. (22) and comparing with the coefficients of Eq. (10) yields

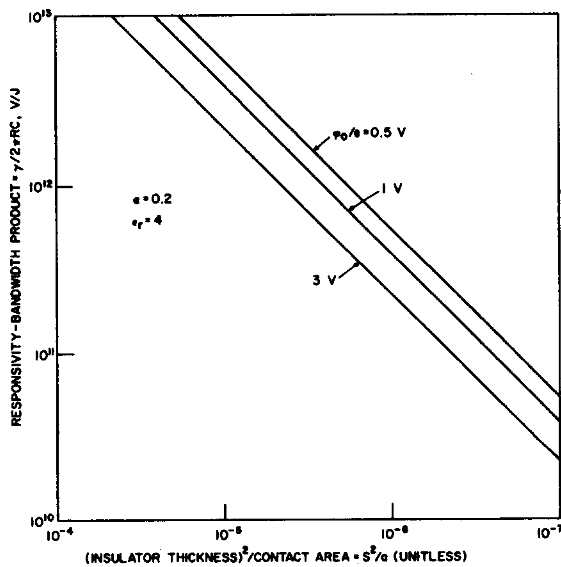

FIG. 6. Responsivity-bandwidth product vs (insulator thickness)²/contact area.

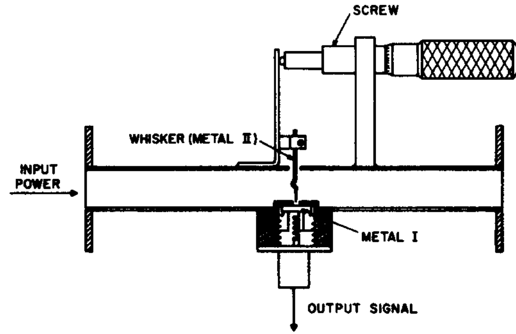

FIG. 7. M-O-M detector waveguide mount.

$$A_0=\exp(-BL^{1/2}),$$

$$A_1=\exp(-BL^{1/2})\left[\frac{B}{4L^{1/2}}+\frac{\Delta\phi B}{48L^{3/2}}\right],$$

$$A_2=\exp(-BL^{1/2})\left[\frac{B}{24L^{3/2}}+\frac{B^2}{32L}+\frac{\Delta\phi B}{64L^{5/2}}+\frac{B^2\Delta\phi}{192L^2}\right]. \quad (23)$$

Evaluation of a_1, a_2, and a_3 involves integrals of the general form

$$\int_0^\eta L^{-(n/2)}\exp(-BL^{1/2})dE_x=-2\int_{(\eta+\phi_0)^{1/2}}^{(\phi_0)^{1/2}}M^{-l}e^{-BM}MdM, \quad (24)$$

where $M=L^{1/2}$ and n, l are integers ≥0. Since $BM^{1/2}\gg1$,[15] the integral can be further approximated [with only negligible effects on Eqs. (26)–(28)] as

$$-2\int_{(\eta+\phi_0)^{1/2}}^{(\phi_0)^{1/2}}M^{-l+1}e^{-BM}dM=-2\int_{\infty}^{(\phi_0)^{1/2}}M^{-l+1}e^{-BM}dM. \quad (25)$$

After lengthy calculations Eqs. (13)–(15) can be expressed as

$$a_1=(2\phi_0/D^2)(D+1)e^{-D}, \quad (26)$$

$$a_2=(De^{-D}\Delta\phi/24\phi_0)[1+DE_i(-D)e^D], \quad (27)$$

and

$$a_3=(De^{-D}/24\phi_0)[1+(DE_i(-D)e^D/2)], \quad (28)$$

where D is defined as

$$D=B\phi_0^{1/2}=4\pi(2m)^{1/2}\phi_0^{1/2}s/h=1.023\hat{s}(\phi_0/e)^{1/2} \quad (29)$$

and $\hat{s}$ is the insulator thickness (Å), (ϕ_0/e) is the average potential (V), and

$$E_i(-D)=\int_\infty^D\frac{e^{-t}}{t}dt.$$

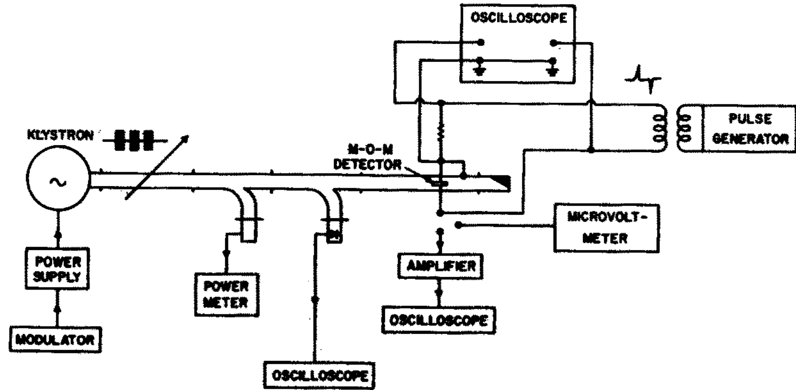

FIG. 8. Experimental setup of the M-O-M detector.

Therefore the current-density equation, Eq. (12), becomes [for $V \ll 4(\phi_0/e)/D$]

$$I_{F,R}=I_0\left[\frac{2\phi_0(D+1)e^{-D}}{D^2}(eV)\pm\frac{\Delta\phi De^{-D}}{24\phi_0}\times[1+DE_i(-D)e^D](eV)^2+\frac{De^{-D}}{24\phi_0}\{1+\tfrac{1}{2}[DE_i(-D)e^D]\}(eV)^3\right], \quad (30)$$

where + corresponds to forward bias and − to reverse bias. In order to compare Eq. (30) with the results obtained by Green[11] the same definitions are used

$$Y=I/J_0\phi_0, \quad \alpha=\Delta\phi/2\phi_0,$$
$$eV/2\phi_0=x, \quad J_0=ea/2\pi hs^2,$$

where a is the contact area. Equation (30) becomes

$$Y_{F,R}=(D+1)e^{-D}\left[x\pm\frac{D^2\alpha}{12(D+1)}[1+DE_i(-D)e^D]x^2+\frac{D^2}{12(D+1)}\{1+\tfrac{1}{2}[DE_i(-D)e^D]\}x^3\right]. \quad (31)$$

Green[11] obtained the following expression:

$$Y_{F,R}=(D-2)e^{-D}\left(x\pm\frac{\alpha D(D-3)}{12(D-2)}x^2+\frac{D}{48(D-2)}\times[2D^2-4D(1\mp2\alpha)-12(1\pm2\alpha)]x^3\right). \quad (32)$$

In the expansion of Eq. (21) the assumption

$$L\gg(\Delta\phi/2)-(\Delta\phi+eV)(x/s)$$

was used, and in particular we set $x=0$ and $E_x=\eta$. This results in the condition

$$\alpha=\Delta\phi/2\phi_0\ll1. \quad (33)$$

Since $D=1.023(\phi_0/e)^{1/2}\hat{s}$, $\hat{s}\gg1$ Å and $\phi_0/e\sim1$ V for practical devices, then

$$D\gg1. \quad (34)$$

Both assumptions (33) and (34) were also employed in Green's work. Under such conditions, $1+DE_i\times(-D)e^D\sim1/D$ as shown in Fig. 3, and both Eqs. (28) and (29) simplify to

$$Y_{F,R}\simeq De^D[x\pm(D\alpha/12)x^2+(D^2/24)x^3]. \quad (35)$$

The assumptions given by Eqs. (33) and (34) do not limit severely the applicability of the theory since the values of ϕ_1 and ϕ_2 are usually close to each other and hence $\alpha=\phi_2-\phi_1/\phi_2+\phi_1\ll1$ is readily satisfied. The film thickness is on the order of 10 Å and ϕ_0/e is on the order of 1 V, hence $D\gg1$ is invariably valid for practical devices.

B. Small-Signal Detection [$V\ll4(\phi_0/e)/D$]

Because the I-V characteristic of M-O-M diodes is nonlinear, it can be used for detection when biased at nonzero voltage. However, detection at no dc bias requires asymmetry in the I-V characteristic. The small-signal I-V characteristic of the M-O-M diode can be expressed as

$$I_{F,R}=(1/R)(V+g_{2F,R}V^2+g_{3F,R}V^3), \quad (36)$$

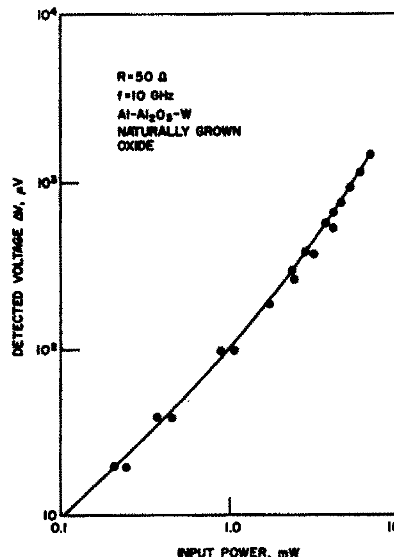

FIG. 9. Responsivity of an M-O-M diode.

where the higher-power terms have been neglected. The subscripts F, R stand for forward and reverse bias, respectively. If a sinusoidal signal $V=V_0\sin\theta$ ($\theta=\omega t$) is applied, the detected dc voltage across the diode is given by

$$\Delta V=\Delta IR$$

$$=(2\pi)^{-1}\left(\int_0^{\pi}(g_{2F}-g_{2R})V^2d\theta+\int_0^{\pi}(g_{3F}-g_{3R})V^3d\theta\right)$$

$$=\tfrac{1}{4}(g_{2F}-g_{2R})V_0^2+2\frac{g_{3F}-g_{3R}}{3\pi}V_0^3. \quad (37)$$

Comparing the coefficients of Eqs. (30) and (36) yields

$$R=[D^2e^Dh^3/8\pi me^2\phi_0(D+1)](1/a), \quad (38)$$

$$g_{2FR}\simeq\pm(\alpha D^2/12)(e/2\phi_0)[1+DE_i(-D)e^D], \quad (39)$$

and

$$g_{3FR}\simeq(D^2/12)(e/2\phi_0)^2\{1+[DE_i(-D)e^D/2]\}. \quad (40)$$

The detected output voltage is then

$$\Delta V\simeq(\alpha D^2/48)(e/\phi_0)[1+DE_i(-D)e^D]V_0^2. \quad (41)$$

The responsivity which is defined as the detected voltage per watt of input power, may then be expressed as

$$\gamma=\frac{\Delta V}{(V_0^2/2R)}=\frac{\alpha D^2}{24}\left(\frac{e}{\phi_0}\right)[1+DE_i(-D)e^D]R. \quad (42)$$

For practical devices $D\gg1$, $1+DE_i(-D)e^D\simeq1/D$ and using $C=\epsilon_r\epsilon_0 a/s$ gives

$$R\simeq3.069\times10^{-15}\frac{\hat{s}}{(\phi_0/e)^{1/2}a}\exp\left[1.023\hat{s}\left(\frac{\phi_0}{e}\right)^{1/2}\right](\Omega), \quad (43)$$

$$RC\simeq2.72\times10^{-16}\frac{\epsilon_r}{(\phi_0/e)^{1/2}}\exp\left[1.023\hat{s}\left(\frac{\phi_0}{e}\right)^{1/2}\right](s) \quad (44)$$

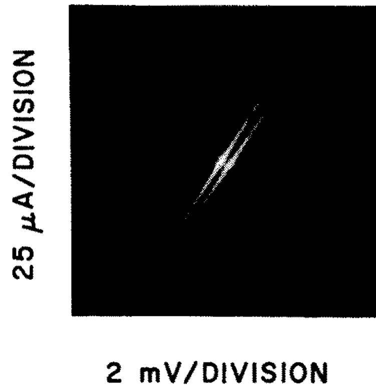

FIG. 10. I–V characteristics of an M–O–M diode. Top: no microwave power. Bottom: microwave power applied.

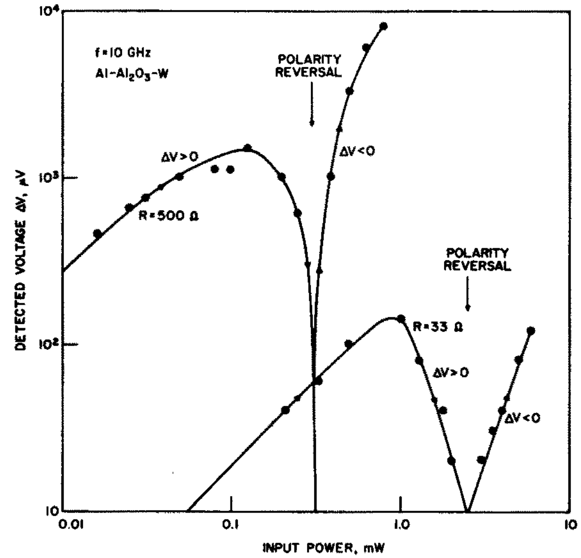

FIG. 11. Responsivity and polarity reversal of M–O–M diodes.

and

$$\gamma\simeq1.31\times10^{-16}\frac{\hat{s}^2\alpha}{a(\phi_0/e)}\exp\left[1.023\hat{s}\left(\frac{\phi_0}{e}\right)^{1/2}\right]\frac{V}{W}. \quad (45)$$

The bandwidth $1/2\pi RC$ and the responsivity of the M–O–M diode are plotted in Figs. 4 and 5. The bandwidth is independent of contact area. It decreases rapidly with increasing film thickness whereas the responsivity increases. Thus we observe the familiar responsivity-bandwidth trade-off relation. The responsivity-bandwidth product is given by the expression

Responsivity-bandwidth product

$$\simeq7.66\times10^{-2}\frac{\hat{s}^2\alpha}{a\epsilon_r(\phi_0/e)^{1/2}}\frac{V}{J}, \quad (46)$$

which is plotted in Fig. 6. It is clear that it is desirable to have a small contact area; increasing the responsivity without trading off the bandwidth.

III. EXPERIMENTAL RESULTS

A. General Description

A polished metal or a metal thin film on the order of 2000 Å evaporated on a piece of glass plate was used as the first metal electrode. The metals used were Al, Sn, and Au. The naturally grown oxide on the surface constitutes the insulator. W and Be–Cu whisker wires which were electroetched to form a sharp tip with a diameter dimension of the order of 1 μm were used as the second electrode. Figure 7 shows the detector mounted in a waveguide. The presence of a micrometer screw allows adjustment of the whisker pressure. At first the whisker is made to contact the film by adjusting the micrometer; then

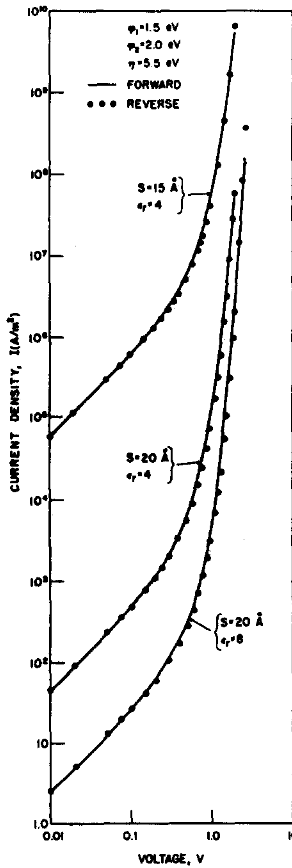

FIG. 12. Calculated I–V characteristics of M–O–M diodes.

the whisker pressure is released slowly. The best detector performance occurs when the whisker is just about to separate from the insulating film. Figure 8 shows the complete experimental setup. The pulsed sweep circuit was connected to the M–O–M diode to observe the I–V characteristic with or without the microwave power applied, without dismantling the setup. Special care must be taken to avoid mechanical vibrations and excessive dc power dissipation, both of which may alter or permanently damage the device. Therefore, the measurements often are not repeatable on a single device. The measurements were taken on different devices.

Figure 9 shows the detector characteristic of a low-resistance Al–Al_2O_3–W diode. At low power levels the diode is essentially a square-law detector; at higher power levels the detector behaves more like a cubic-law device. As will be seen later from more exact calculations carried out on a computer, this is characteristic of the M–O–M detector. In Fig. 10, the irradiated I–V characteristic of the same diode exhibits both a voltage offset and a slope offset. The voltage offset is characteristic of a square-law device and the slope offset is due to cubic terms. This is consistent with the responsivity of Fig. 9.

B. Polarity Reversal

Figure 11 shows the responsivity of two M–O–M detectors having resistances of 500 and 33 Ω, respectively. As is evident from Eqs. (38) and (42) it is expected that the diode with a higher resistance will have a higher responsivity; this fact is borne out experimentally in Fig. 11. Also evident from the experimental data is that the polarity of the detected voltage reverses at a certain power level. This large-signal polarity reversal is often accompanied by an unstable detected signal. In some devices no such phenomenon was observed, e.g., Fig. 9, but presumably the polarity would reverse at a higher power level.

Clearly, the small-signal theory using a trapezoidal potential barrier precludes this large-signal phenomenon. (See Appendix A for a slightly perturbed trapezoidal potential barrier.) This polarity reversal may be expected from the large-signal I–V characteristic of a M–O–M structure with two dissimilar electrodes.

IV. MORE EXACT COMPUTER CALCULATIONS OF THE I–V CHARACTERISTICS

In view of the failure of the small-signal theory to explain the deviation of the responsivity from the square-law characteristic and the large-signal polarity reversal, a more exact calculation is desirable. Using a realistic approximation of the image potential due to Simmons,[2] namely,

$$\phi_i = -[1.15s^2/x(s-x)]\lambda \tag{47}$$

and

$$\lambda = e^2 \ln 2/8\pi\epsilon s. \tag{48}$$

The current densities can be expressed as,

$$I_F = \frac{4\pi m e}{h^3}\bigg[\int_0^{\eta-eV} eV \exp\bigg(-\frac{4\pi}{h}\times\int_{s_1}^{s_2}[2m(\phi_F+\eta-E_x)]^{1/2}dx\bigg)dE_x + \int_{\eta-eV}^{\eta}(\eta-E_x)\times\exp\bigg(-\frac{4\pi}{h}\int_{s_1}^{s_2}[2m(\phi_F+\eta-E_x)]^{1/2}dx\bigg)dE_x\bigg] \tag{49}$$

and

$$I_R = \frac{4\pi m e}{h^3}\bigg[\int_0^{\eta-eV} eV \exp\bigg(-\frac{4\pi}{h}\times\int_{s_1'}^{s_2'}[2m(\phi_R+\eta-E_x)]^{1/2}dx\bigg)dE_x + \int_{\eta-eV}^{\eta}(\eta-E_x)\times\exp\bigg(-\frac{4\pi}{h}\int_{s_1'}^{s_2'}[2m(\phi_R+\eta-E_x)]^{1/2}dx\bigg)dE_x\bigg], \tag{50}$$

where s_1, s_2, s_1', and s_2' are the classical turning points. s_1 and s_2 are the real roots of

$$\phi_F = \phi_2 - (\phi_2 - \phi_1 + eV)(x/s) + \phi_i = 0; \tag{51}$$

s_1' and s_2' are the real roots of

$$\phi_R=\phi_1-(\phi_1-\phi_2+eV)(x/s)+\phi_i=0. \quad (52)$$

Equations (49) and (50) have been programmed on a computer for evaluation. In order to avoid a triple integration when calculating the detected current density, the following approximation[2] on the exponent integral in Eqs. (49) and (50) is made[2]:

$$\int_{s_1}^{s_2}(\phi_F+\eta-E_x)^{1/2}dx=(\bar{\phi}_F+\eta-E_x)^{1/2}$$

$$\times\int_{s_1}^{s_2}\left[1-\frac{1}{8}\left(\frac{\phi_F-\bar{\phi}_F}{\bar{\phi}_F+\eta-E_x}\right)^2\right]dx, \quad (53)$$

where

$$\bar{\phi}_F=(s_2-s_1)^{-1}\int_{s_1}^{s_2}\phi_F dx, \quad (54)$$

and similarly for the reverse-bias case.

The I–V characteristics for $\phi_2=2$ eV and $\phi_1=1.5$ eV with different insulating film thicknesses and dielectric constants are given in Fig. 12. It is noted that the reverse current is invariably close or smaller in magnitude than that of the forward bias for small voltages. However at a voltage level near ϕ_2 the reverse current becomes larger, and increases rapidly with a higher voltage. If a large sinusoidal signal is applied to the diode, the rectified current will reverse its polarity when the reverse current dominates at large voltage swings, causing polarity reversal of the detected signal. The current density increases quite rapidly with decreasing insulator width. The effect of the image potential tends to reduce both the potential barrier height as well as width, hence increasing the current density. Since the image potential is inversely proportional to the dielectric constant of the insulating film, increasing the dielectric constant reduces the current density. In the limit when $\epsilon_r\rightarrow\infty$ the current density corresponds to that obtained from a trapezoidal potential barrier.

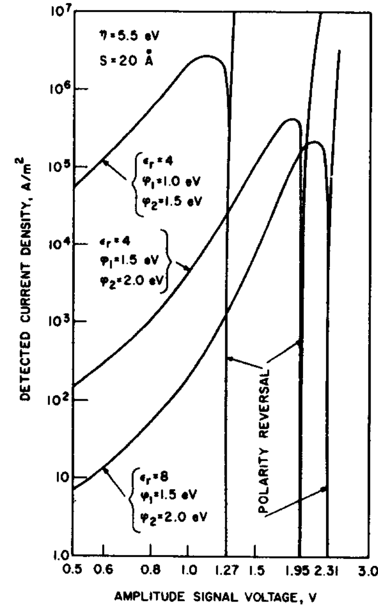

FIG. 14. Expanded scale of calculated responsivity near the polarity-reversal point.

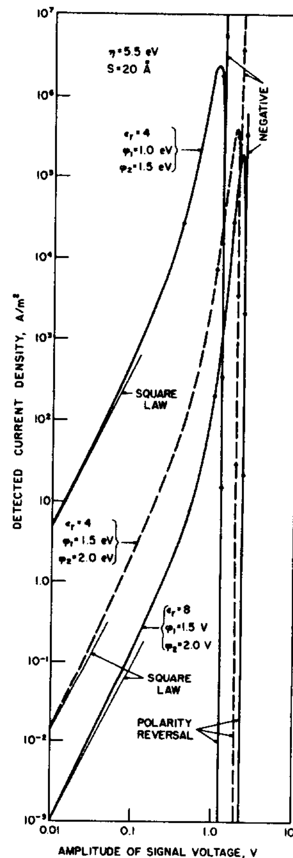

FIG. 13. Calculated responsivity of M–O–M diodes.

A. Detected Current Density

The detected current density has been calculated by evaluating the following integral:

$$\Delta I=(2\pi)^{-1}\left(\int_0^{\pi} I_F(V_0\sin\theta)d\theta-\int_0^{\pi} I_R(V_0\sin\theta)d\theta\right). \quad (55)$$

In order to avoid excessive computing time, an accuracy to three decimal places was imposed on the value of the detected current density. The results are plotted in Fig. 13. An expanded scale near the polarity-reversal point is shown in Fig. 14. There are several noteworthy observations:

(1) The M–O–M detector obeys approximately a square law at low signal levels, and gradually the higher terms dominate at larger levels before the eventual polarity reversal occurs.

(2) Polarity reversal takes place at a voltage level close to the value of ϕ_2/e (the larger work function).

(3) The effect of the image potential (as can be seen through the change of dielectric constant) causes polarity reversal at a lower signal level. This effect however is not as significant as when ϕ_2 is varied.

(4) The detected current increases rapidly with decreasing ϕ_0.

(5) The detected current increases rapidly with decreasing film thickness s.

As noted in Fig. 13 the detected current deviates from square law significantly, however, such a trend is not proportionately reflected on the responsivity plots (Figs. 9 and 11). The detected voltage was measured across the diode and its resistance is known to decrease rapidly with a large voltage, thus countering the effect of a current increase. Another detection scheme where the detected current is monitored should give better agreement with the theoretical results. The fact that the polarity reversal occurs at a lower power level for an M–O–M diode having a higher resistance is readily explained from the result that $V_{0r} \sim \phi_2/e$ which is relatively constant while R varies over a wide range. Thus $P = V_{0r}^2/2R$ will vary with R.

V. CONCLUSIONS

Small-signal calculations of the I–V characteristics and the detection properties of an M–O–M structure using an idealized trapezoidal barrier by the expansion of the transmission coefficient

$$D(E_x) = A_0(E_x) + A_1(E_x)(eV) + A_2(E_x)(eV)^2$$

and

$$I = I_0[a_1(eV) + a_2(eV)^2 + a_3(eV)^3]$$

yield results which are in good agreement with the work of Green[11] who used the generalized I–V relation of Simmons.[2–4]

The small-signal theory predicts the M–O–M structure to be a square-law detector which agrees fairly well with the observed characteristics at small-signal levels. The analysis reveals the essential detector properties such as responsivity, bandwidth and the responsivity-bandwidth product as functions of the device parameters: work functions of the metals, thickness of the insulating film, dielectric constant of the film and the contact area. No calculations at $T \neq 0°$K were attempted. For room temperature applications, the thermal effect on the I–V characteristic is not significant[4] and hence will not affect the detection properties either.

The above small-signal calculations preclude the experimental large-signal polarity reversal of the detected signal. However, if a small perturbation is added to the trapezoidal barrier as an artificial image potential the calculations show the possibility of such a polarity reversal, though the quantitative prediction is inadequate.

More realistic computer calculations which include the image potential explain the deviation of the detector responsivity from that of a square law. The large-signal polarity reversal was estimated to take place when the applied voltage is close to ϕ_2/e, ϕ_2 being the larger work function of the two metals. The experimentally observed phenomenon that the polarity reversal occurs at a lower power level for an M–O–M diode having a higher resistance can also be explained from the results.

APPENDIX A: SMALL-SIGNAL ANALYSIS OF A SLIGHTLY PERTURBED TRAPEZOIDAL BARRIER

Assume a perturbed trapezoidal barrier as shown in Fig. 15, then

$$\phi_F = \phi_2 - \beta + 4\beta[1-(x/s)](x/s) - (\Delta\phi + eV)(x/s)$$
$$= \phi_0 + \tfrac{1}{2}(\Delta\phi) - \beta + 4\beta[1-(x/s)](x/s) - (\Delta\phi + eV)(x/s) \quad (56)$$

and

$$\phi_R = \phi_0 + \left(-\frac{\Delta\phi}{2}\right) - \beta + 4\beta\left(1-\frac{x}{s}\right)\frac{x}{s} - (-\Delta\phi + eV)\frac{x}{s}, \quad (57)$$

where β is the perturbation parameter $\ll \phi_0$. In the limit $\beta \to 0$ Eqs. (56) and (57) become the same as Eqs. (17) and (18), respectively.

Performing similar calculations as before, keeping the terms proportional to $\Delta\phi$, eV, $\Delta\phi eV$, $(eV)^2$, $\Delta\phi(eV)^2$ and discarding β^2 and higher terms, we have corresponding to Eqs. (21) and (23)

$$\rho_\beta = -BL^{1/2}\left\{\left(1-\frac{\beta}{6L}\right) - \left[\left((4L)^{-1} + \frac{\beta}{24L^2}\right) + \left((48L^2)^{-1} + \frac{3\beta}{160L^3}\right)\Delta\phi\right](eV) - \left[\left((24L^2)^{-1} + \frac{\beta}{40L^3}\right) + \Delta\phi\left((64L^3)^{-1} + \frac{3\beta}{128L^4}\right)\right](eV)^2\right\} \quad (58)$$

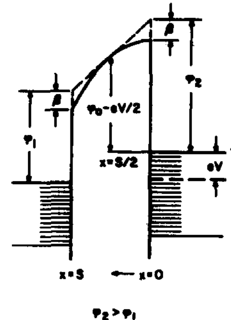

FIG. 15. Perturbed trapezoidal barrier.

and

$$A_{0\beta} \simeq A_0 + \beta \exp(-BL^{1/2})(B/6L^{1/2}),$$

$$A_{1\beta} \simeq A_1 + \beta \exp(-BL^{1/2}) \left[\left(\frac{B}{24L^{3/2}} + \frac{B^2}{24L} \right) + \Delta\phi \left(\frac{3B}{160L^{5/2}} + \frac{B^2}{288L^2} \right) \right],$$

$$A_{2\beta} \simeq A_2 + \beta \exp(-BL^{1/2}) \left[\left(\frac{B}{40L^{5/2}} + \frac{5B^2}{288L^2} + \frac{B^3}{192L^{3/2}} \right) + \Delta\phi \left(\frac{3}{128} \frac{B}{L^{7/2}} + \frac{47B^2}{640 \times 9L^3} + \frac{B^3}{6 \times 192L^{5/2}} \right) \right]. \quad (59)$$

Finally for $D \gg 1$, $1 + DE_i(-D)e^D \approx 1/D$ the following is obtained

$$a_1 \simeq (2\phi_0/D^2)(D+1)e^{-D},$$

$$a_2 \simeq \beta \frac{De^{-D}}{12\phi_0} \pm \frac{\Delta\phi}{24\phi_0} e^{-D} \left[1 + \frac{3}{10} D \left(\frac{\beta}{\phi_0} \right) \right],$$

$$a_3 \simeq \frac{De^{-D}}{\phi_0} \left[\frac{1}{48} + \left(\frac{\beta}{\phi_0} \right) \frac{D}{60} \left(\frac{45}{4} - \frac{13}{24} D \right) \mp \left(\frac{\beta}{\phi_0} \right) \frac{\Delta\phi}{160\phi_0} \right]. \quad (60)$$

The detected voltage can be expressed as

$$\Delta V \simeq \frac{\alpha D}{48} \left(\frac{e}{\phi_0} \right) \left[1 + \frac{3}{10} D \left(\frac{\beta}{\phi_0} \right) \right] V_0^2 \left(1 - \frac{V_0}{V_{0r}} \right), \quad (61)$$

where, for small perturbations, $D(\beta/\phi_0) \leqq 1$ the following is obtained

$$V_{0r} \simeq \tfrac{5}{2}\pi(\phi_0/\beta)(\phi_0/e)D^{-1}. \quad (62)$$

Taking a favorable case $D(\beta/\phi_0) \sim 1$ then $V_{0r} \sim (5\pi/2)(\phi_0/e)$ which is about five times higher than ϕ_2/e, a result predicted from the computer calculations.

* This work was partially supported by the Electronics Research Center of the National Aeronautics and Space Administration under Grant No. NGL 23-005-18.3

† G. Lobov was visiting at the Electron Physics Laboratory during 1968–1969. He is presently with the Moscow Power Engineering Institute, Moscow, U.S.S.R.

[1] R. Holm, J. Appl. Phys. **22**, 569 (1951).
[2] J. G. Simmons, J. Appl. Phys. **34**, 1793 (1963).
[3] J. G. Simmons, J. Appl. Phys. **35**, 2472 (1964).
[4] J. G. Simmons, J. Appl. Phys. **35**, 2655 (1964).
[5] R. Stratton, J. Phys. Chem. Solids **22**, 1177 (1962).
[6] T. E. Hartman, J. Appl. Phys. **33**, 3427 (1962).
[7] D. R. Fredkin and G. H. Wannier, Phys. Rev. **128**, 2054 (1962).
[8] K. K. Thornber, T. C. McGill, and C. A. Mead, J. Appl. Phys. **38**, 2384 (1967).
[9] C. Lewicki and C. A. Mead, Phys. Rev. Lett. **16**, 939 (1966).
[10] L. O. Hocker, D. R. Sokoloff, V. Daneu, A. Szoke, and A. Javan, Appl. Phys. Lett. **12**, 401 (1968).
[11] S. I. Green, Ph.D. thesis, University of Illinois, 1969.
[12] P. D. Coleman and S. I. Green, IEEE Int. Electron Devices Meeting, 1968.
[13] E. Merzbacher, *Quantum Mechanics* (Wiley, New York, 1961), Chap. 7.
[14] Expand Eq. (12) in a Taylor series of eV first.
[15] Assuming $BM^{1/2} \gg 1$ and $\eta > \phi_0$, both of which are true for practical M–O–M structures.